

Low-Field Metal-Insulator Transition in AB-Stacked Bilayer Graphene

Amarnath Chakraborty,^{1,*} Aleksandr Rodin,^{2,3,4,†} Shaffique Adam,⁵ and Giovanni Vignale^{6,‡}

¹*Department of Physics and Astronomy, University of Missouri, Columbia, Missouri, USA*

²*Yale-NUS College, 16 College Avenue West, 138527, Singapore*

³*Centre for Advanced 2D Materials, National University of Singapore, 117546, Singapore*

⁴*Department of Materials Science and Engineering,
National University of Singapore, 9 Engineering Drive 1, 117575, Singapore*

⁵*Department of Physics, Washington University in St. Louis, St. Louis, Missouri 63130, United States*

⁶*The Institute for Functional Intelligent Materials (I-FIM),*

National University of Singapore, 4 Science Drive 2, Singapore 117544

(Dated: March 27, 2026)

We investigate the interplay of in-plane magnetic and transverse electric fields in AB-stacked bilayer graphene. In prior work, we demonstrated that this configuration induces an insulator-metal (IM) transition with large impact on the magnetic response, albeit requiring impractically large magnetic fields. Here, we extend the analysis by incorporating previously neglected trigonal warping effects through interlayer skew couplings. In a restricted region of momentum space (on the order of 1/100 of the original Brillouin zone) trigonal warping produces a fine splitting of Dirac cones leading to a compensated semimetallic state in the absence of external fields. Application of a transverse electric field above a small threshold ($V_c \sim 0.6$ meV) reinstates the insulating gap, but this gap can be closed by a relatively small in-plane magnetic field, leading to an IM transition at a much smaller magnetic field (≈ 10 T) than previously predicted.

I. INTRODUCTION

The electronic and magnetic properties of graphene systems under magnetic fields have long been a topic of great interest in solid state physics. In monolayer graphene, perpendicular magnetic fields produce striking phenomena such as relativistic Landau levels [1], integer [2] and fractional [3] quantum Hall effects, and gate-tunable orbital magnetism.

Bilayer graphene (BLG) offers an even richer scenario. Interlayer coupling and stacking geometry enable mechanical, electrical, and magnetic control over band topology. For instance, twisted bilayer graphene hosts flat bands that give rise to superconductivity and correlated insulating states [4], while Bernal-stacked bilayers exhibit gate-tunable bandgaps [5] and orbital magnetism sensitive to in-plane magnetic fields (B_{\parallel}) [6, 7]. The latter arises because B_{\parallel} couples asymmetrically to the two layers, shifting their uncoupled band structures in opposite momentum directions. When interlayer hybridization is activated, this generates reconstructed Fermi surfaces and anomalous orbital responses [8].

On the other hand, the low-energy distortion of the Fermi surface induced by interlayer skew couplings (γ_3 ,

γ_4) in the Slonczewski–Weiss–McClure model [9, 10] renormalizes the Fermi velocity and imparts a threefold symmetry to the band structure [5, 11, 12]. Quantum-Hall experiments at low carrier density report an eightfold degeneracy of the lowest Landau level—consistent with a parabolic dispersion and spin, valley, and orbital symmetries [2, 13, 14]—in contrast tight-binding models that include skew hoppings (γ_3, γ_4) predict a gapless fine structure featuring four mini-Dirac cones and van Hove singularities at modest displacement fields [13, 15, 16]. Moreover, large E_{\perp} opens sizable gaps and yields anomalous quantum-Hall sequences in BLG [17–20], as well as in Bernal trilayer graphene [21–23], rhombohedral trilayer graphene [24, 25], and Bernal tetralayer graphene [26], consistent with a trigonally warped low-energy Fermi surface.

Recently, Seiler *et al.* [5] investigated the fine structure of trigonal warping under an applied displacement field, both theoretically and experimentally, addressing the long-standing absence of clear signatures of linearly dispersing bands and electric-field-driven topological transitions in BLG. By combining high-field magnetotransport measurements on hBN-encapsulated bilayer graphene with realistic tight-binding modeling [27], they identified signatures of band-structure reconstruction associated with a van Hove singularity. In particular, the emergence of four Dirac cones leads to an unconventional sequence of Landau levels, distinct from the previously established picture.

* amarnathchakraborty95@gmail.com

† aleksandr.rodin@yale-nus.edu.sg

‡ vgnl.g@nus.edu.sg

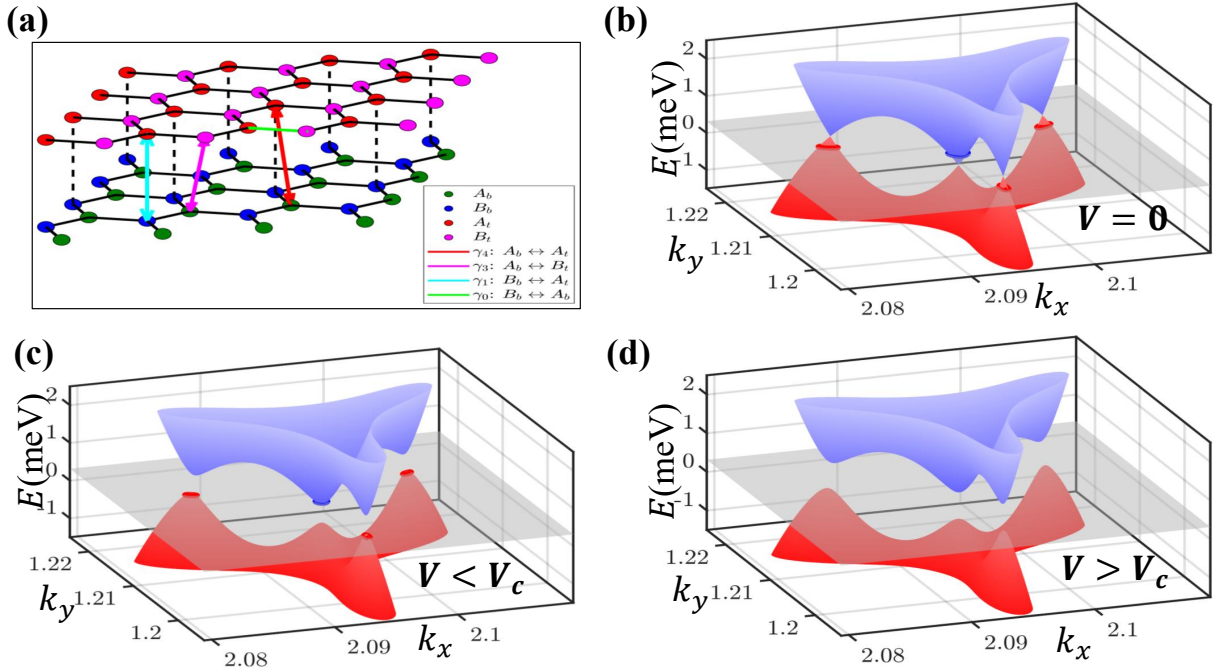


FIG. 1: AB-stacked bilayer graphene lattice and band structure with trigonal warping. (a) Side view of the AB-stacked lattice showing relevant interlayer hopping terms. (b) Semi-metallic state at zero field with $E_F = 0.313$ meV. (c) Semi-metallic state with displacement field slightly below the critical value. (d) Insulating state achieved by exceeding the critical displacement field.

Despite these advances, the combined effects of an in-plane magnetic field (B_{\parallel}) and a transverse electric field (E_{\perp}) in the presence of trigonal warping remain largely unexplored. Here we focus on the low-energy regime near the mini-Dirac pockets, where the relevant scales are set by the skew hoppings (γ_3 and γ_4). In our prior work [28], we showed that B_{\parallel} and E_{\perp} together can drive an insulator-metal (IM) transition in AB-stacked bilayer graphene: E_{\perp} opens a gap, while B_{\parallel} hybridizes layer-polarized states and closes it above a critical field B_c . However, that analysis neglected trigonal warping and consequently predicted $B_c \gtrsim 100$ T, well beyond experimental reach. Here we extend that study by incorporating skew hoppings into full tight-binding simulations of the B_{\parallel} - E_{\perp} transition (Fig. 1a-b). Focusing on the low-energy Fermi surface within roughly 1% of the Brillouin zone (within ~ 1 meV of the Dirac points), we confirm that at zero magnetic field the system evolves from a gapless semimetal at $E_{\perp} = 0$ to a gapped insulator above a critical displacement field, consistent with Ref. [5]. We then show that a much smaller in-plane magnetic field can close this gap. Compared with the unwarped case [28], trigonal warping lowers the critical field dramatically,

bringing it from over 100 T to ~ 10 T, a range accessible to modern cryogenic magnetotransport experiments [29]. At very large B_{\parallel} , warping effects become negligible as the Fermi surface coalesces into a single anisotropic pocket, recovering the high-field behavior reported in our earlier study [28].

Therefore, building on the experimental accessibility of the trigonal-warped regime demonstrated by Seiler *et al.*, our work goes one step further by showing how this system responds to an additional in-plane magnetic field. In particular, we predict a field-tuned re-entrant insulator-metal transition beyond the effect of the displacement field alone. More broadly, these results highlight trigonal warping as a key lever for graphene-based magnetoelectronic device design and show that low-energy band topology, shaped by skew couplings, can be engineered through crossed electric and magnetic fields.

II. TIGHT BINDING MODEL

The Bernal-stacked graphene bilayer is described by a tight-binding Hamiltonian with nearest-neighbor intra-

and interlayer hopping [30]

$$H_{\mathbf{k}} = \begin{pmatrix} -V/2 & \gamma_0 f(\mathbf{k}_t) & \gamma_4 f(\mathbf{k}) & \gamma_3 f^*(\mathbf{k}) \\ \gamma_0 f^\dagger(\mathbf{k}_t) & -V/2 + \Delta & \gamma_1 & \gamma_4 f(\mathbf{k}) \\ \gamma_4 f^*(\mathbf{k}) & \gamma_1 & V/2 + \Delta & \gamma_0 f(\mathbf{k}_b) \\ \gamma_3 f(\mathbf{k}) & \gamma_4 f^*(\mathbf{k}) & \gamma_0 f^\dagger(\mathbf{k}_b) & V/2 \end{pmatrix} \quad (1)$$

The four basis states are A_t , B_t , A_b , and B_b with A and B denoting the sublattice and t/b subscripts identifying the top and bottom layers. The hopping energy between B_t and A_b is $\gamma_1 = 0.361\text{eV}$, while the hopping term between the nearest neighbors within a layer is $\gamma_0 = -2.61\text{eV}$ [5, 27]. Here $f(\mathbf{k}) = \sum_{n=1}^3 e^{i\mathbf{k}\cdot\boldsymbol{\delta}_n}$, where $\boldsymbol{\delta}_1 = a(-1, \sqrt{3})/2$, $\boldsymbol{\delta}_2 = a(-1, -\sqrt{3})/2$, and $\boldsymbol{\delta}_3 = a(1, 0)$ are the vectors connecting atoms A to their nearest neighbors within a layer and $a \approx 1.42\text{\AA}$ is the carbon bond length in graphene. The diagonal terms $\pm V$ originate from an external electric field applied perpendicular to the bilayer (the displacement field). In addition to the nearest-neighbor intralayer hopping energy, we also include the skew interlayer couplings $\gamma_3 = -0.283\text{ eV}$, $\gamma_4 = 0.138\text{ eV}$ and the energy difference between dimer and non-dimer sites $\Delta = 0.015\text{ eV}$ [5, 27]. Finally, the constant vector potential enters the Hamiltonian via the Peierls substitution $\mathbf{k} \rightarrow \mathbf{k} \pm e\mathbf{A}/\hbar$, so that we have

$$\mathbf{k}_{t/b} a = \mathbf{k} a \pm \pi\Phi(\sin\theta, -\cos\theta, 0), \quad (2)$$

where l is the interlayer separation and $\Phi = Bal/\Phi_0$ is the magnetic flux through a rectangle defined by an in-plane bond and an inter-plane segment in units of the magnetic flux quantum $\Phi_0 = h/e \simeq 4.14 \times 10^5\text{ T}\cdot\text{\AA}^2$. Here $\theta = \pi/2$ corresponds to a vector potential parallel to the x -axis (zig-zag direction) and a magnetic field parallel to the y -axis (armchair direction). Notice that the skew-coupling terms do not carry the Peierls phase as they describe a motion in the z -direction, which is not affected by the in-plane vector potential.

III. ACCESSIBLE IM TRANSITION ENABLED BY TRIGONAL WARPING

In our previous work [28], we analyzed the insulator-semimetal transition in AB-stacked bilayer graphene at half filling under a transverse field E_\perp and an in-plane magnetic flux Φ , modeling each layer as a Dirac cone displaced vertically by $\pm V$ and horizontally by $\Delta\mathbf{k} = \Phi/a$. By including only the interlayer coupling γ_1 , we found that the system is gapped with a gap $2\gamma_1$ independent of V and remains gapped as long as

$$\gamma_1 < 3\pi|\gamma_0|\Phi$$

and transitions to a compensated semimetal when this inequality is violated, i.e., when Φ exceeds the critical value

$$\Phi_c = \frac{\gamma_1}{3\pi|\gamma_0|}, \quad (3)$$

corresponding to very large field $B_c \approx 100\text{ T}$ (with an auxiliary P-strain).

In the present work, we show that the trigonal-warping terms dramatically changes the scenario. First of all, the system, at $V = 0$, is not an insulator but a semimetal. Following Ref.[11] one can show that at low-energy the trigonal warping fragments the Fermi surface into one central pocket (conduction band) and three satellite pockets (valence band) around each K point (Fig. 1(b)). By resolving the band structure on a scale of $1/100^{\text{th}}$ of the original Brillouin zone (BZ), one uncovers threefold-symmetric Dirac cones (Fig. 1(c)) which cross the Fermi level, giving rise to a semimetallic state. Applying a perpendicular displacement field E_\perp gaps the central Dirac cone at zero energy but leaves the warped pockets intact, so the system remains semimetallic until

$$V_c \approx 0.63\text{ meV}. \quad (4)$$

This fundamentally alters the scenario of the magnetic field induced insulator-metal (IM) transition. Below V_c , residual valence-band pockets sustain a finite density of states at the Fermi level (shifted to $E_F \approx 0.31\text{ meV}$ by particle-hole asymmetry from γ_4), whereas for $V > V_c$ all pockets are gapped and a full bulk gap appears (Fig. 1d). The small insulating gap can be closed by a relatively small in-plane magnetic field ($\approx 10T$), leading to an IM transition, as we discuss in the following sections.

A. Critical displacement field and gap opening

We extract V_c by direct diagonalization of the full tight-binding Hamiltonian on a dense k -grid, tracking the minimum indirect gap via Eq. (5). Because V_c depends sensitively on the skew-hopping ratio γ_3/γ_1 , our results suggest that strain or dielectric engineering could tune the threshold, offering an additional control parameter for low-field IM transitions.

This behavior has two key implications. First, it highlights the necessity of including skew-hopping terms (γ_3, γ_4) when modeling low-energy transport and optics: below V_c , the ungapped pockets dominate conductivity and yield anisotropic cyclotron orbits in quantum-oscillation measurements. Second, the Berry-curvature textures of these warped pockets—even prior to full gap

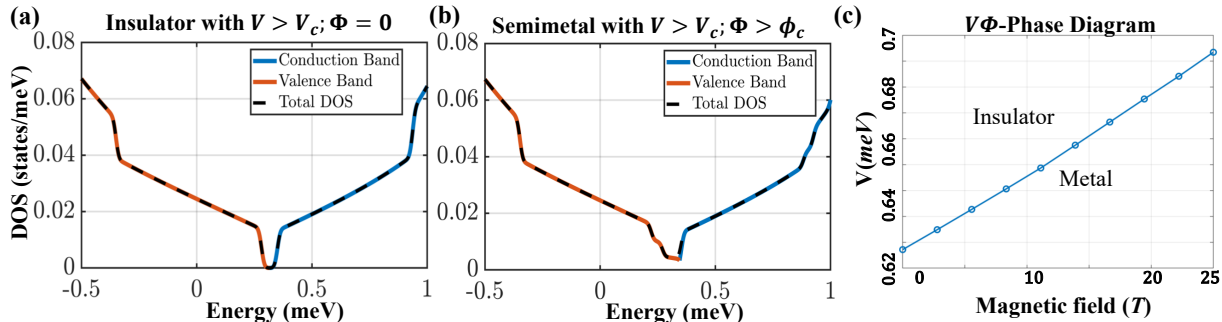


FIG. 2: Density of states across the metal–insulator transition. (a) Insulating state for $V > V_c$ with vanishing DoS. (b) Semi-metallic state restored by in-plane magnetic field $\phi > \phi_c$. (c) V – ϕ phase diagram showing the critical magnetic field for gap closure, with cutoff at 25 T.

opening—may drive pronounced valley-Hall or nonlinear Hall responses that switch sharply at V_c .

With V_c established as the “zero-field” gap threshold, we can now explore how an in-plane magnetic flux Φ further suppresses or closes the gap, thereby tracing out the IM phase boundary in the (V, Φ) plane.

B. Phase boundary determination

To investigate the metal–insulator transition we first examine the density of states (DoS) under different external field configurations, as shown in Fig. 2. When the displacement field V exceeds the critical value V_c , the DoS at the Fermi level vanishes, signalling the opening of a full bandgap and the onset of an insulating phase (Fig. 2(a)). Applying an in-plane magnetic field ϕ above a critical threshold ϕ_c closes this gap, producing a finite DoS at the Fermi level and restoring a semi-metallic phase (Fig. 2(b)). To capture the complete transition, we construct a V – ϕ phase diagram beginning at $V = V_c$ and extending to $V \approx 0.71$ meV, indicating the critical magnetic field required for gap closure at each displacement field. For relevance to current experiments, we limit the field range to $B \leq 25$ T (Fig. 2(c)).

With the phase boundary determined, we convert the critical flux into a physical field via $B_c(V) = \Phi_c(V) \Phi_0 / (a\ell)$, where $\Phi_0 = h/e$ and ℓ is the interlayer spacing. When trigonal warping is included the estimated critical field falls to the $\mathcal{O}(10$ T) range — roughly two orders of magnitude smaller than the unwarped estimate ($B_c \gtrsim 10^3$ T). This dramatic reduction has a numerical signature through an abrupt jump of the density of states at the Fermi level once $\Phi > \Phi_c(V)$, signaling the sudden formation of compensated electron–hole pockets.

To map out the insulating and semimetallic regions in

the (V, Φ) plane, for each (V, Φ) we diagonalize H and extract the two middle eigenvalues using the full Hamiltonian (Eq. 1) such that:

$$E_2(\mathbf{k}; V, \Phi) \leq E_3(\mathbf{k}; V, \Phi),$$

$E_2(\mathbf{k}; V, \Phi)$ is the energy at the top of the valence band and $E_3(\mathbf{k}; V, \Phi)$ is the energy at the bottom of the conduction band. We define the gap

$$E_g(V, \Phi) = \min_{\mathbf{k}} [E_3(\mathbf{k}; V, \Phi) - E_2(\mathbf{k}; V, \Phi)]. \quad (5)$$

By convention, $E_g > 0$ corresponds to an insulator, while $E_g \leq 0$ signals a compensated semimetal. For fixed Φ , we scan V in small increments, compute $E_g(V)$ via Eq. (5), and interpolate between successive points to locate the critical displacement $V_c(\Phi)$ at which $E_g = 0$. Repeating this procedure for various Φ constructs the phase-boundary curve $V_c(\Phi)$ illustrated in Fig. 2(c).

Quantitatively, we find that in the low-energy regime a displacement field $V > V_c$ opens an indirect gap, defined as the difference between the minimum of the conduction band and the maximum of the valence band $E_{c,min} - E_{v,max} = \Delta(V) \propto V - V_c$; but an in-plane magnetic field closes this gap by promoting interlayer hybridization. This behavior differs qualitatively from our earlier high-energy analysis, where the zero-B (magnetic field) indirect gap was essentially set by the interlayer coupling γ_1 and insensitive to V . In the present, warped low-energy bandstructure the zero-B gap is parametrically smaller (fractions of a meV rather than hundreds of meV) and scales with $V - V_c$ rather than being fixed by γ_1 .

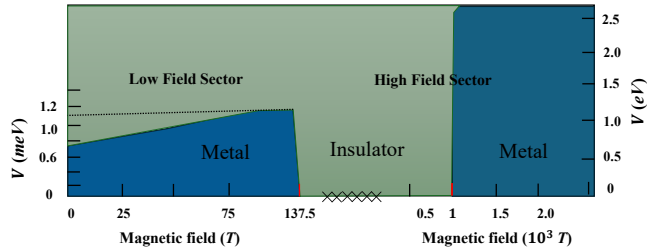


FIG. 3: Phase diagram showing the insulating (green) and metallic (blue) regions in the (V, Φ) plane. The low-field sector (this work) exhibits an insulator–metal (IM) boundary driven by a finite displacement V and an in-plane flux Φ ; color axes are indicated on the left (meV) and right (eV). A crossover near ~ 137.5 T marks where the trigonal-warping picture breaks down; beyond this crossover one recovers the high-field regime discussed in Ref. [28], where the unwarped model predicts a much larger critical field (~ 1000 T).

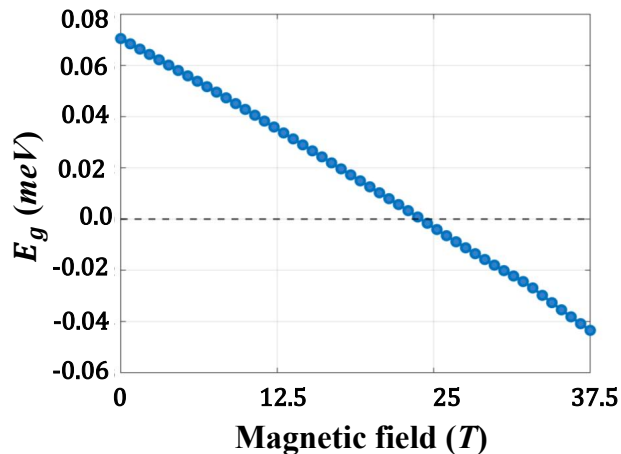


FIG. 4: At displacement field $V > V_c$: 0.7meV . Evolution of the indirect band-gap E_g with respect to applied in-plane magnetic field strength ϕ . Shows almost linearly decreasing nature with increasing magnetic field.

C. Magnetic field dependence of the energy gap

It is useful to parametrize the field dependence of the gap by the magnetic-field induced momentum shift. Denoting by k_B the characteristic momentum displacement produced by the in-plane field (with $k_B \propto eB\ell/\hbar$, where ℓ is the interlayer spacing), the leading effect of the field on the gap can be written as (see Fig. 4)

$$E_g(B) = E_g(0) - \alpha \hbar v k_B, \quad (6)$$

where $E_g(0) \equiv \Delta(V)$, v is the relevant Dirac velocity near the pockets, and $\alpha \gtrsim 1$ is a dimensionless coefficient that

encapsulates details of the pocket geometry and interlayer overlap. Equation (6) captures the linear closing of the gap with field observed in our numerics.

Setting $E_g(B_c) = 0$ yields an analytic estimate for the critical field,

$$B_c = \frac{E_g(0)}{\alpha \hbar v} \frac{\hbar}{e\ell} \propto E_g(0) \propto (V - V_c). \quad (7)$$

Thus, because $E_g(0) \propto V - V_c$ in the trigonal-warped low-energy regime, B_c acquires an approximately linear dependence on the displacement field. This explains our observation in Fig. 2 that B_c grows roughly linearly with $V - V_c$ (e.g. reaching $B_c \sim 25$ T at $V \approx 0.71$ meV in the parameter set used here), and it also clarifies why the required fields are orders of magnitude smaller than the unwarped estimate.

While Fig. 2(c) shows the phase diagram in the relevant, low-magnetic field region, for completeness we also show the full phase diagram in Fig. (3), spanning both the low- and high-field regimes; with an emphasis the crossover to the high-field (or high-momentum) regime. The low-field sector — the focus of this paper — exhibits an insulator–metal (IM) transition driven by a finite displacement V and an in-plane flux Φ (or B_{\parallel}). This IM transition persists up to a magnetic field on the order of 10^2 T (≈ 137.5 T in our parameter set); beyond this scale k_B exceeds the characteristic trigonal-warping momentum k_w [31], the pocket picture breaks down, and the band structure evolves to a single anisotropic pocket that is gapped by V (i.e., a bulk insulator) and the phase boundary should saturate toward the constant-field behavior (on the right side of Fig. 3) found in our previous high-energy study [28]. Notice that the left vertical axis reports energies in meV (useful for low-energy, warped physics) while the right vertical axis shows the same scale in eV (convenient for connecting to high-energy, zone-averaged estimates). The low-energy section of this phase diagram is entirely controlled by trigonal warping.

In short, including trigonal warping both (i) reduces the zero-field gap (via γ_4 and the pocket structure) and (ii) converts the IM critical field from a V -independent constant into an approximately linear function of $V - V_c$, with a crossover back to the earlier constant- B_c result at sufficiently large in-plane magnetic field.

D. Effect of Zeeman coupling

Conspicuously absent from our discussion so far has been the effect of Zeeman coupling, which shifts the energies of opposite spins by $\pm\mu_B B$ (with $\mu_B = e\hbar/2m$), independently of momentum. In the convention used here the

down-spin band is pushed downward by $-\mu_B B$ while the up-spin band is pushed upward by $+\mu_B B$. As a result the spin-resolved separations between conduction and valence extrema are modified as

$$E_{c,\min}(\downarrow) - E_{v,\max}(\uparrow) = E_g(B) - 2\mu_B B = E_g(B) - \frac{e\hbar B}{m}, \quad (8)$$

and

$$E_{c,\min}(\uparrow) - E_{v,\max}(\downarrow) = E_g(B) + 2\mu_B B = E_g(B) + \frac{e\hbar B}{m}, \quad (9)$$

where $E_g(B)$ denotes the spinless (orbital) gap including orbital-field effects. Because one channel is reduced by $2\mu_B B$, the net effect of Zeeman coupling is making the system more semimetallic at zero displacement field. Thus, a larger displacement field is required to open a spin-degenerate bulk gap. In other words, Zeeman shifts produce a small upward renormalization of the critical displacement V_c needed to convert the warped semimetal into a full insulator.

This statement can be quantified by comparing the Zeeman scale $2\mu_B B \sim e\hbar B/m$ with the orbital field term responsible for gap closing, which in our phenomenology scales as $\sim (\alpha v_F e B \ell)/(2\pi)$. Their ratio is

$$\frac{e\hbar B/m}{(\alpha v_F e B \ell)/(2\pi)} \sim \frac{\hbar}{mv_F \ell} \frac{2\pi}{\alpha} \sim \frac{a}{\alpha \ell},$$

where a is the in-plane bond length and we used $\hbar/(mv_F) \sim a$ parametrically. This makes the Eq. (6) and Eq. (8) be combined as:

$$E_g(B) = E_g(0) - \alpha \hbar v k_B - \frac{e\hbar B}{m}, \quad (10)$$

$$= E_g(0) - \alpha \hbar v k_B (1 + \frac{a}{\alpha \ell}) \quad (11)$$

The Zeeman contribution thus appears merely as an additive correction to E_g (equivalently a tiny shift of V_c), and it does not alter the orbital mechanism that closes the V -dependent gap. With $a/\ell \approx 0.3$ and $\alpha \gtrsim 1$ (in practice $\alpha > 1$ in the warped, low-energy regime) this ratio is small. Even in the conservative case $\alpha \simeq 1$, the Zeeman correction to the required transition field is modest; for realistic parameters it is essentially negligible.

We therefore conclude that Zeeman coupling increases the threshold displacement V_c slightly (because it makes the unperturbed system more semimetallic), but the resulting fractional change of the critical in-plane field is small in the parameter range studied. Accordingly, Zeeman effects do not alter our principal conclusion that trigonal warping renders the IM transition experimentally accessible.

IV. DISCUSSION AND CONCLUSION

In this work we have demonstrated that including trigonal-warping terms (γ_3, γ_4) in the tight-binding description of AB-bilayer graphene under crossed in-plane (B_{\parallel}) and displacement (E_{\perp}) fields leads to an insulator-semimetal (IM) transition at magnetic fluxes and field strengths an order of magnitude smaller than previously predicted. While earlier high-field treatments—neglecting skew couplings—yielded critical fields $B_c \gtrsim 100$ T, we find $B_c \sim 10$ T once low-energy warping distorts the Fermi surface into four mini-Dirac pockets of finite interlayer overlap. The dramatic reduction of B_c arises because trigonal warping (γ_3) reconstructs the low-energy spectrum into mini-Dirac pockets where the interlayer form factor is finite, allowing efficient hybridization at much smaller in-plane momentum shifts. Concurrently, the skew coupling γ_4 breaks particle-hole symmetry and unpins the pocket energies which further reduces the required B_c .

Our full tight-binding calculations (Fig. 1) confirm that for $\Phi < \Phi_c$ the system remains a gapped insulator, whereas for $\Phi > \Phi_c$ compensated electron-hole pockets immediately appear. Importantly, Φ_c varies only weakly with the direction of the applied in-plane field, owing to the threefold symmetry of the warped pockets, and remains within the reach of modern cryogenic magneto-transport facilities [29]. This behavior contrasts with our previous high-energy analysis, where the critical magnetic field was found to be independent of the applied electric field, yielding a constant B_c for all V . The present low-energy treatment reveals an almost linear dependence of B_c on V , which we expect to saturate once the magnetic-field-induced momentum shift exceeds the characteristic scale set by trigonal warping. At that point, the phase boundary should converge to the constant-field result from our earlier study.

These findings open several exciting avenues for future exploration. Experimentally, gated bilayer-graphene devices can now be probed in pulsed or hybrid magnets up to ~ 30 T to directly observe the predicted gap closing via measurements of longitudinal conductivity, thermopower, and quantum oscillations [32]. The threefold-mini-pocket topology also suggests the possibility of tuning carrier imbalance between pockets by suitable strain or twist, enabling controlled studies of multi-valley hydrodynamics and two-fluid transport [33].

Finally, the central role of skew-hopping-induced warping in lowering B_c raises the prospect that other two-dimensional moiré and multilayer systems, where skew couplings are inherently strong, may exhibit similarly accessible IM transitions. For instance, trilayer graphene,

transition-metal dichalcogenide bilayers, and twisted heterostructures could be engineered to exploit warping-facilitated band inversions at modest fields. By revealing how low-energy geometrical distortions can govern field-driven phase boundaries, our study provides a blueprint for engineering tunable semimetallic states in van der Waals materials. In addition, since our earlier work identified a diamagnetic-to-paramagnetic crossover in the high-energy regime, it is natural to ask how this orbital response evolves in the present low-energy, trigonal-warped setting. Although we do not analyze it here, the reconstructed pocket structure suggests that the magnetic susceptibility can be substantially renormalized in the warped regime. This remains an interesting direction for

future work.

We thank Leonid Levitov for bringing to our attention Ref. [5], which motivated this work. We also thank Carsten Ullrich for a useful discussion on the role of the Zeeman coupling, and Guang Bian for many useful discussions. A.C. was supported by the U.S. Department of Energy, Office of Science, Office of Basic Energy Sciences, Division of Materials Science and Engineering, under Grant No. DE-SC0024294. G.V. was supported by the Ministry of Education, Singapore, under its Research Centre of Excellence award to the Institute for Functional Intelligent Materials (I-FIM, Project No. EDUNC-33-18-279-V12).

-
- [1] Y. Zhang, Y.-W. Tan, H. L. Stormer, and P. Kim, Experimental observation of the quantum hall effect and berry's phase in graphene, *Nature* **438**, 201 (2005).
- [2] K. S. Novoselov, E. McCann, S. V. Morozov, V. I. Fal'ko, M. I. Katsnelson, U. Zeitler, D. Jiang, F. Schedin, and A. K. Geim, Unconventional quantum hall effect and berry's phase of 2π in bilayer graphene, *Nature Physics* **2**, 177 (2006).
- [3] K. I. Bolotin, F. Ghahari, M. D. Shulman, H. L. Stormer, and P. Kim, Observation of the fractional quantum hall effect in graphene, *Nature* **462**, 196 (2009).
- [4] Y. Cao, V. Fatemi, S. Fang, K. Watanabe, T. Taniguchi, E. Kaxiras, and P. Jarillo-Herrero, Unconventional superconductivity in magic-angle graphene superlattices, *Nature* **556**, 43 (2018).
- [5] A. M. Seiler, N. Jacobsen, M. Statz, N. Fernandez, F. Falorsi, K. Watanabe, T. Taniguchi, Z. Dong, L. S. Levitov, and R. T. Weitz, Probing the tunable multi-cone band structure in bernal bilayer graphene, *Nature Communications* **15**, 3133 (2024).
- [6] M. Kammermeier, P. Wenk, and U. Zülicke, In-plane magnetoelectric response in bilayer graphene, *Phys. Rev. B* **100**, 10.1103/physrevb.100.075421 (2019).
- [7] W.-Y. He, Y. Su, M. Yang, and L. He, Creating in-plane pseudomagnetic fields in excess of 1000 t by misoriented stacking in a graphene bilayer, *Phys. Rev. B* **89**, 125418 (2014).
- [8] J. M. Park, Y. Cao, L.-Q. Xia, S. Sun, K. Watanabe, T. Taniguchi, and P. Jarillo-Herrero, Robust superconductivity in magic-angle multilayer graphene family, *Nature Materials* **21**, 877 (2022).
- [9] J. C. Slonczewski and P. R. Weiss, Band structure of graphite, *Phys. Rev.* **109**, 272 (1958).
- [10] J. W. McClure, Theory of diamagnetism of graphite, *Phys. Rev.* **119**, 606 (1960).
- [11] E. McCann and M. Koshino, The electronic properties of bilayer graphene, *Reports on Progress in Physics* **76**, 056503 (2013).
- [12] M. Mucha-Kruczyński, E. McCann, and V. I. Fal'ko, Electron-hole asymmetry and energy gaps in bilayer graphene, *Semiconductor Science and Technology* **25**, 033001 (2010).
- [13] R. T. Weitz, M. T. Allen, B. E. Feldman, J. Martin, and A. Yacoby, Broken-symmetry states in doubly gated suspended bilayer graphene, *Science* **330**, 812 (2010), <https://www.science.org/doi/pdf/10.1126/science.1194988>.
- [14] A. S. Mayorov, D. C. Elias, M. Mucha-Kruczynski, R. V. Gorbachev, T. Tudorovskiy, A. Zhukov, S. V. Morozov, M. I. Katsnelson, V. I. Fal'ko, A. K. Geim, and K. S. Novoselov, Interaction-driven spectrum reconstruction in bilayer graphene, *Science* **333**, 860 (2011), <https://www.science.org/doi/pdf/10.1126/science.1208683>.
- [15] K. S. Novoselov, A. K. Geim, S. V. Morozov, D. Jiang, M. I. Katsnelson, I. V. Grigorieva, S. V. Dubonos, and A. A. Firsov, Two-dimensional gas of massless dirac fermions in graphene, *Nature* **438**, 197 (2005).
- [16] B. Partoens and F. M. Peeters, From graphene to graphite: Electronic structure around the k point, *Phys. Rev. B* **74**, 075404 (2006).
- [17] E. McCann and V. I. Fal'ko, Landau-level degeneracy and quantum hall effect in a graphite bilayer, *Phys. Rev. Lett.* **96**, 086805 (2006).
- [18] A. M. Seiler, F. R. Geisenhof, F. Winterer, K. Watanabe, T. Taniguchi, T. Xu, F. Zhang, and R. T. Weitz, Quantum cascade of correlated phases in trigonally warped bilayer graphene, *Nature* **608**, 298 (2022).
- [19] H. Zhou, L. Holleis, Y. Saito, L. Cohen, W. Huynh, C. L. Patterson, F. Yang, T. Taniguchi, K. Watanabe, and A. F. Young, Isospin magnetism and spin-polarized superconductivity in bernal bilayer graphene, *Science* **375**, 774 (2022), <https://www.science.org/doi/pdf/10.1126/science.abm8386>.
- [20] A. Varlet, M. Mucha-Kruczyński, D. Bischoff, P. Simonet, T. Taniguchi, K. Watanabe, V. Fal'ko, T. Ihn, and K. En-

- sslin, Tunable fermi surface topology and lifshitz transition in bilayer graphene, *Synthetic Metals* **210**, 19 (2015), reviews of Current Advances in Graphene Science and Technology.
- [21] A. A. Zibrov, P. Rao, C. Kometter, E. M. Spanton, J. I. A. Li, C. R. Dean, T. Taniguchi, K. Watanabe, M. Serbyn, and A. F. Young, Emergent dirac gullies and gully-symmetry-breaking quantum hall states in *aba* trilayer graphene, *Phys. Rev. Lett.* **121**, 167601 (2018).
- [22] F. Winterer, A. M. Seiler, A. Ghazaryan, F. R. Geisenhof, K. Watanabe, T. Taniguchi, M. Serbyn, and R. T. Weitz, Spontaneous gully-polarized quantum hall states in *aba* trilayer graphene, *Nano Letters* **22**, 3317 (2022).
- [23] L. C. Campos, A. F. Young, K. Surakitbovorn, K. Watanabe, T. Taniguchi, and P. Jarillo-Herrero, Quantum and classical confinement of resonant states in a trilayer graphene fabry-pérot interferometer, *Nature Communications* **3**, 1239 (2012).
- [24] H. Zhou, T. Xie, A. Ghazaryan, T. Holder, J. R. Ehrets, E. M. Spanton, T. Taniguchi, K. Watanabe, E. Berg, M. Serbyn, and A. F. Young, Half- and quarter-metals in rhombohedral trilayer graphene, *Nature* **598**, 429 (2021).
- [25] H. Zhou, T. Xie, T. Taniguchi, K. Watanabe, and A. F. Young, Superconductivity in rhombohedral trilayer graphene, *Nature* **598**, 434 (2021).
- [26] Y. Shi, S. Che, K. Zhou, S. Ge, Z. Pi, T. Espiritu, T. Taniguchi, K. Watanabe, Y. Barlas, R. Lake, and C. N. Lau, Tunable lifshitz transitions and multiband transport in tetralayer graphene, *Phys. Rev. Lett.* **120**, 096802 (2018).
- [27] J. Jung and A. H. MacDonald, Accurate tight-binding models for the π bands of bilayer graphene, *Phys. Rev. B* **89**, 035405 (2014).
- [28] A. Chakraborty, A. Rodin, S. Adam, and G. Vignale, Insulator-metal transition and magnetic crossover in bilayer graphene, *Phys. Rev. B* **111**, 125130 (2025).
- [29] H. Zhou, L. Holleis, Y. Saito, L. Cohen, W. Huynh, C. L. Patterson, F. Yang, T. Taniguchi, K. Watanabe, and A. F. Young, Isospin magnetism and spin-polarized superconductivity in bernal bilayer graphene, *Science* **375**, 774 (2022), <https://www.science.org/doi/pdf/10.1126/science.abm8386>.
- [30] A. H. Castro Neto, F. Guinea, N. M. R. Peres, K. S. Novoselov, and A. K. Geim, The electronic properties of graphene, *Rev. Mod. Phys.* **81**, 109 (2009).
- [31] Where k_w is the characteristic momentum scale of trigonal warping (the distance of the mini-pockets from the central cone [11]).
- [32] Y. Zhao, P. Cadden-Zimansky, Z. Jiang, and P. Kim, Symmetry breaking in the zero-energy landau level in bilayer graphene, *Phys. Rev. Lett.* **104**, 066801 (2010).
- [33] D. Y. H. Ho, I. Yudhistira, N. Chakraborty, and S. Adam, Theoretical determination of hydrodynamic window in monolayer and bilayer graphene from scattering rates, *Phys. Rev. B* **97**, 121404 (2018).